arXiv:astro-ph/0502519v1 24 Feb 2005

Energetics in MRI driven Turbulence

Thomas A. Gardiner* and James M. Stone*

*Department of Astrophysical Sciences, Princeton University, Princeton, NJ 08544

Abstract. In these proceedings we present recent efforts to understand the energetics of magnetohydrodynamic (MHD) turbulence driven by the magneto-rotational instability (MRI). These studies are carried out in the local (shearing box) approximation using the Athena simulation code. Athena is a higher order Godunov algorithm based on the piecewise parabolic method (PPM), the corner transport upwind (CTU) integration algorithm, and the constrained transport (CT) algorithm for evolving the magnetic field. This algorithm is particularly suited for these studies owing to the conservation properties of a Godunov scheme and the particular implementation of the shearing box source terms used here. We present a variety of calculations which may be compared directly to previously published results and discuss them in some detail. The only significant discrepancy found between the results presented here and in the published literature involves the turbulent heating rate. We observe the presence of recurrent channel solutions in calculations involving a mean vertical magnetic field and the associated time lag between the energy injection and thermalization rate. We also present the results of a shearing box calculation which includes an optically thin radiative term with a cooling rate selected to match the turbulent heating rate. Some properties which we find uniformly present in all of the calculations presented here are compressible fluctuations, spiral waves and weak shocks. It is found that these compressible modes dominate the temporal fluctuations in the probability distribution functions for most of the thermodynamic variables; only the specific entropy is relatively immune to their effects.

Keywords: MHD; accretion disks
PACS: 95.30.Qd; 97.10.Gz

INTRODUCTION

The last 10 years have borne witness to a substantial improvement in our understanding of the role of sub-thermal magnetic fields in accretion disk physics [1]. The magneto-rotational instability (MRI) plays the central role in driving magnetohydrodynamic (MHD) turbulence which in turn transports mass and angular momentum. A large body of work now exists in the literature which has elucidated a great many aspects of the MRI. Yet surprisingly, one aspect of accretion disk physics has yet to receive significant attention; this is the role of energetics [2, 3, 4].

One of the simplest energetics questions which could be addressed with numerical simulations is, what energy reservoir is tapped, how is the energy distributed amongst its kinetic and magnetic forms, and where does it ultimately go. Some elements of this question have been answered repeatedly by a number of researchers. The differential rotation is the ultimate energy source which is tapped via the MRI and injected into the kinetic and magnetic energy. The energy stored in the form of magnetic and kinetic energy may be exchanged [5], but ultimately, it is dissipated and ends up as thermal heating. Interestingly enough, this last stage is relatively unimportant as far as the MRI itself is concerned since there is only a weak pressure dependence on the growth rates [6] and saturation amplitudes [7]. Nevertheless, it is the last stage of this process

which results in radiation and allows a comparison between theoretical calculations and observations.

There are two circumstances under which the thermal state of the plasma can be easily understood to have a significant impact on an MRI turbulent accretion disk. The first is in determining the vertical structure of a stratified accretion disk. The scale height of an accretion disk is determined by balancing the thermal pressure gradients against gravity. The disk scale height is thus a measure of the mean or central gas pressure, and is determined directly from the balance of turbulent heating (as well as other potential sources) and radiative losses. (This is a question we intend to explore in the near future.) The second is by the strong temperature dependence on the ionization state, resistivity, and other kinetic effects which directly modify the induction equation such as ambipolar diffusion or the Hall conductivity. For example, the degree to which the MRI plays a role in protostellar accretion will depend heavily on these factors [8, 9]. It has also been suggested that the temperature sensitivity of the resistivity could serve as a *switch* which regulates the outburst activity in dwarf nova disks [10, 11].

The focus of this paper is twofold with the ultimate goal to seek a better understanding of the energetics in MRI turbulent accretion disks. This goal is ultimately achievable as a result of the recent development of a fully second order accurate, conservative Godunov algorithm for ideal MHD [12]. Using the shearing box formalism, one is assured that any energy injected into the computational domain ultimately results in thermally heating the plasma without directly modeling the physical dissipation processes. Nevertheless, since this is a new computational algorithm, and is the first time that a fully second order Godunov algorithm has been applied to the study of the MRI we are compelled to repeat a series of calculations which can be directly compared with published results. The second goal of this paper is to validate this new computational algorithm when applied to the study of MRI driven MHD turbulence in the shearing box and to understand any differences which arise between the results presented here and published in the literature. To that end, we present results for adiabatic calculations with three different field geometries and a calculation including radiative cooling.

NUMERICAL CALCULATIONS

Shearing Box Approximation

The studies presented here make use of the local "shearing box" formalism [13]. In this approach, one focuses on a local section of an accretion disk at some fiducial radius R_0 and in a reference frame co-rotating at the local angular velocity Ω_0. Expanding the ideal MHD system of equations in cylindrical coordinates for small deviations $\delta r/R_0 \ll 1$, etc. and relabeling the coordinates $(dr, R_0 d\phi, dz)$ as (dx, dy, dz) one obtains the ideal MHD system in a Cartesian domain plus and additional set of source terms which represent the Coriolis and tidal gravity forces. For a Keplerian accretion disk one obtains

$$\frac{\partial \rho}{\partial t} + \nabla \cdot (\rho \mathbf{v}) = 0 \tag{1}$$

$$\frac{\partial \rho \mathbf{v}}{\partial t} + \nabla \cdot (\rho \mathbf{v}\mathbf{v} - \mathbf{B}\mathbf{B}) + \nabla P^* = \rho \Omega_0^2 (3x\hat{i} - z\hat{k}) - 2\Omega_0 \hat{k} \times \rho \mathbf{v} \quad (2)$$

$$\frac{\partial \mathbf{B}}{\partial t} + \nabla \cdot (\mathbf{v}\mathbf{B} - \mathbf{B}\mathbf{v}) = 0 \quad (3)$$

$$\frac{\partial E}{\partial t} + \nabla \cdot ((E + P^*)\mathbf{v} - \mathbf{B}(\mathbf{B} \cdot \mathbf{v})) = \Omega_0^2 \rho \mathbf{v} \cdot (3x\hat{i} - z\hat{k}) \quad (4)$$

where ρ is the mass density, $\rho\mathbf{v}$ is the momentum density, $\mathbf{B}$ is the magnetic field, and E is the total energy density. The total pressure $P^* \equiv P + (\mathbf{B} \cdot \mathbf{B})/2$ where P is the gas pressure, and the total energy density E is related to the internal energy density ε via

$$E \equiv \varepsilon + \rho(\mathbf{v} \cdot \mathbf{v})/2 + (\mathbf{B} \cdot \mathbf{B})/2 \, . \quad (5)$$

This system of equations is closed with an equation of state relating the pressure to the density and internal energy. We use an ideal gas equation of state for which $P = (\gamma - 1)\varepsilon$, and take $\gamma = 5/3$. In the calculations presented in this paper we further simplify this system of equations by neglecting the vertical z-component of gravity. As a result, the calculations presented here are applicable to the central ~ 1 scale height of the accretion disk.

We present calculations both with and without radiative cooling. In those calculations which include optically thin radiative cooling we choose a simple form for the cooling term which is appropriate for bremsstrahlung radiation. In these cases we add a term to the right hand side of equation (4) of the form

$$-A\rho^2(\varepsilon/\rho)^{1/2} \quad (6)$$

and choose the coefficient A such that the cooling rate matches the turbulent heating rate.

Numerical Method

The numerical method we use to solve the MHD equations in the shearing box approximation can be described as having three basic parts. These are the basic integration algorithm, the treatment of source terms within this algorithm and the application of the boundary conditions. We briefly describe each of these in turn in what follows.

Integration Algorithm

We solve the shearing box system of MHD equations using the recently developed simulation code, Athena. This code was constructed to solve the system of ideal hydrodynamics (HD) and magnetohydrodynamics (MHD) by combining a few key algorithms. The integration algorithm is based upon the directionally unsplit corner transport upwind (CTU) integration algorithm of Collela [14, 15]. The CTU integration algorithm can be formally understood as a procedure for correcting the interface states in the piecewise parabolic method (PPM) [16] to account for multidimensional wave propagation.

We have combined this algorithm with the method of constrained transport (CT) [17] to evolve the magnetic field and explicitly preserve the $\nabla \cdot \mathbf{B} = 0$ condition. A detailed description of the construction of this integration algorithm for MHD in two dimensions is in press [12] and a description of the three dimensional algorithm is in preparation.

At the time of this writing, detailed code verification calculations, user and programmer's guides, download information, etc. can be found on the Athena home page at `http://www.astro.princeton.edu/~jstone/athena/`. See also the article by J. Stone in these proceedings for more information on the Athena integration algorithm and a description of the first application results.

Source Terms

One of our principal goals in this work is to study the energetics in MRI turbulent accretion disks. Hence, the evolution of the energy equation (4) is of particular interest. Energy conservation can be restored to this system of equations by solving for the evolution of the *total* energy $E_t = (E + \rho\Phi)$, including the tidal potential, $\Phi = -1.5\Omega_0^2 x^2$. With this choice, one is guaranteed by the conservative nature of the equations, that energy can be exchanged between its kinetic, magnetic, and thermal forms, but cannot be lost in the form of truncation error. The only route by which energy can be added to or removed from the computational domain is through the boundaries. In fact, making use of the shearing periodic boundary conditions one can show [13] that the volume average of the total energy $< E + \rho\Phi >$ evolves as

$$\frac{\partial}{\partial t} < E + \rho\Phi >= \frac{1.5\Omega_0}{L_y L_z} \int_X (\rho v_x \delta v_y - B_x B_y)\, dydz \tag{7}$$

where $\delta v_y = v_y + 1.5\Omega_0 x$ is the angular velocity fluctuation, and the integral is taken over one of the bounding x-faces. This is precisely the route by which the MRI taps the kinetic energy in the form of differential rotation in the shearing box and amplifies the magnetic field. In the calculations presented here, the integral relation in equation (7) is satisfied to numerical roundoff error.

We have found that the treatment of the source terms in the momentum equation (3) is particularly important for shearing box calculations with Athena. Note that unlike the energy equation, the momentum equation cannot be recast in a conservative form. Moreover, there is a simple limit in which the x- and y-momentum equations are *strongly* coupled via the source terms and therefore should not be evolved independently. This strong coupling limit describes the solution for uniform epicyclic oscillation modes. For epicyclic oscillations there is a conserved kinetic energy

$$E_{epi} = \frac{1}{2}\rho \left(v_x^2 + 4(\delta v_y)^2 \right) \ . \tag{8}$$

We have found that implementing the source terms in Athena in such a way that the epicyclic kinetic energy is conserved is extremely important.

In order to clarify why the conservation of the epicyclic kinetic energy should have such a large impact on the solution, note that it is the long wavelength modes which

contain a dominant share of the energy. This is a natural consequence of the shearing box formalism in which the driving scale is effectively equal to the radial size of the computational domain and the dissipation which occurs in the form of a turbulent cascade. In addition to long wavelength modes which fit into the computational domain, the shearing box MHD equations (and boundary conditions) also support uniform epicyclic oscillation modes. It is reasonable to expect that some coupling between long wavelength modes (which fit in the computational domain) and epicyclic oscillation modes may result from numerical truncation error. By conserving the epicyclic kinetic energy, one ensures that this coupling can not set up a positive feedback loop amplifying the kinetic energy in the box.

In order to conserve the epicyclic kinetic energy we evolve not the *y*-momentum equation, but the equivalent conservation law for the angular momentum fluctuation $\rho\delta v_y$. When written in this form, uniform epicyclic motion is consistent with the vanishing of the flux gradient terms. This leaves the *x*- and *y*-momentum fluctuations evolution to be controlled by the resulting source terms. One can show that evaluating the source terms using Crank-Nicholson preserves the epicyclic kinetic energy.

For those calculations which include radiative cooling, we apply the operator splitting technique and split the radiative cooling equation

$$\frac{\partial \varepsilon}{\partial t} = -A\rho^2(\varepsilon/\rho)^{1/2} \tag{9}$$

from the rest of the shearing box evolution equations and solve for the radiative cooling at constant density.

Boundary Conditions

The boundary conditions which we employ in these calculations are strictly periodic in the *y*- and *z*-directions and shearing periodic in the *x*-direction. One result of these boundary conditions is that so long as the volume averaged *x*-component of the magnetic field is zero, the mean flux through the computational domain is fixed in time. The implementation of the boundary conditions in this work preserves this condition to roundoff error for the *x*- and *z*-components of the magnetic field and to truncation error for the *y*-component of the magnetic field. Moreover, the remapping of the magnetic field in the ghost zones at the *x*-boundaries of the computational domain preserves the $\nabla \cdot \mathbf{B} = 0$ condition to roundoff error. The details of how this is achieved will be described in a future paper.

RESULTS

In this section we will present results from three local shearing box simulations with different magnetic field geometries. The cases which we consider here include a mean toroidal field, a mean vertical field, and a zero net-flux case. Our choice of computational domain and initial conditions mirrors that used in [13]. Namely, we choose a computational domain given by $-0.5 \leq x \leq 0.5$, $-\pi \leq y \leq \pi$, $-0.5 \leq z \leq 0.5$ and resolve it on

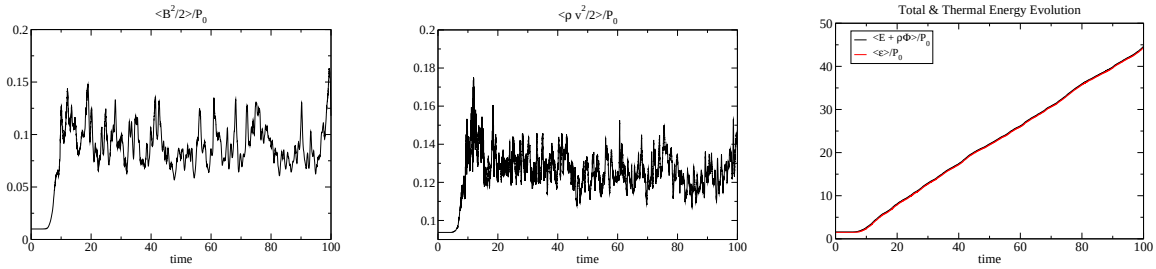

FIGURE 1. Time evolution of the volume averaged magnetic, kinetic, total and thermal energy for the mean toroidal field calculation Y2. Time is in units of the orbital period.

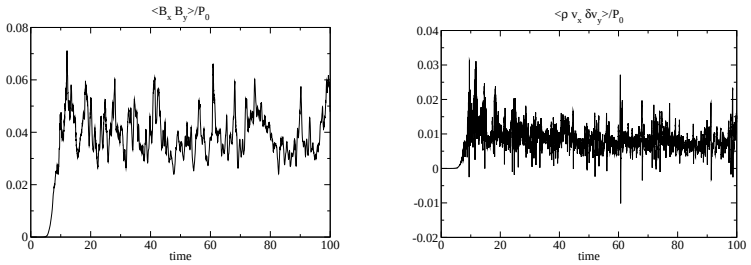

FIGURE 2. Time evolution of the volume averaged Maxwell and Reynolds stress for the mean toroidal field calculation Y2. Time is in units of the orbital period.

a $64 \times 128 \times 64$ grid, except where stated otherwise. The initial velocity components $v_x = v_z = 0$ and $v_y = -1.5\Omega_0 x$. We also choose $\Omega_0 = 10^{-3}$, the initial density $\rho = 1$ and pressure $P = 10^{-6}$. To these initial conditions we add 0.1% white noise adiabatic density and pressure perturbations. For reference, in the following analysis we choose the zero point of the tidal potential $\Phi = (0.125 - 1.5x^2)\Omega_0^2$ so that initially the mean tidal potential energy $< \rho\Phi >= 0$.

Uniform Toroidal Magnetic Field

The first case we consider has an initial magnetic field given by $B_x = B_z = 0$ and $B_y = const.$ with $\beta = 2P/B^2 = 100$. This model calculation can be compared directly to models Y1 and Y11 in [13]. In figure 2 we present the time history of the volume averaged Maxwell and Reynolds stress. The volume averaged Maxwell stress $< -B_x B_y > /P_0$ and Reynolds stress $< \rho v_x \delta v_y > /P_0$ have a mean value of $0.040 \pm 8.0 \times 10^{-3}$ and $8.7 \times 10^{-3} \pm 3.4 \times 10^{-3}$ respectively where the error is given by one standard deviation. The ratio of the Maxwell to Reynolds stress is ~ 4.4. These values are in good agreement with the results of [13]. Similarly we find that the saturation value for the kinetic and magnetic energy density shown in figure 1 are in good agreement with the results of [13].

The results presented here differ from those in [13] when we consider the evolution of the thermal energy density. In figure 1 we present the evolution of the volume averaged thermal energy density $< \varepsilon >$ and the total energy density $< E + \rho\Phi >$. As noted

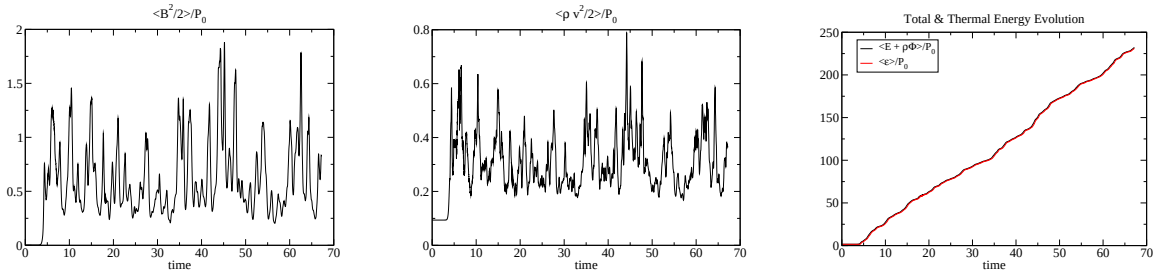

FIGURE 3. Time evolution of the volume averaged magnetic, kinetic, total and thermal energy for the mean vertical field calculation Z2. Time is in units of the orbital period.

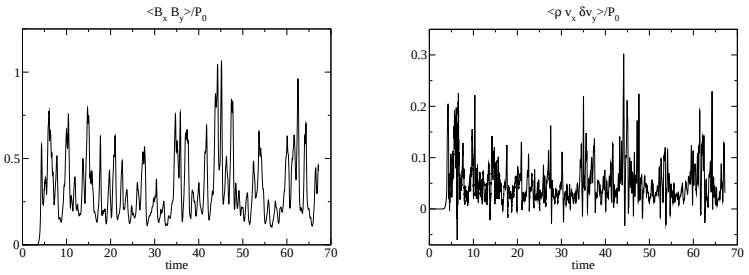

FIGURE 4. Time evolution of the volume averaged Maxwell and Reynolds stress for the mean vertical field calculation Z2. Time is in units of the orbital period.

previously, the total energy in the shearing box is conserved and its volume average can increase only through the differences of the flux across the radial boundaries. From figure 1 we see that the internal and total energies track one another very closely as they must after the kinetic and magnetic energy densities reach saturation. Applying a linear curve fit to the evolution of the total energy density after saturation and applying equation (7), one may extract the surface averaged value of the Maxwell plus Reynolds stress one finds a very good agreement with the volume averages noted above. When compared to the results in [13] we find that the turbulent heating rate is increased by nearly an order of magnitude. This difference is likely attributable to the lack of a resistive heating term in the evolutionary equation for the internal energy.

Uniform Vertical Magnetic Field

Next we consider the case where the magnetic field is initialized with $B_x = B_y = 0$ and $B_z = const.$ with $\beta = 2P/B^2 = 400$. This model calculation can be compared directly to models Z4, Z7, Z19 and Z22 in [13]. In figure 3 we present the temporal evolution of the volume averaged kinetic, magnetic, thermal and total energies, and in figure 4 the Maxwell and Reynolds stress. It is immediately apparent upon inspection that this field configuration is much more time variable as a result of recurrent channel flows [18]. The volume averaged Maxwell stress $< -B_x B_y > /P_0$ and Reynolds stress $< \rho v_x \delta v_y > /P_0$ have a mean value of 0.33 ± 0.18 and 0.051 ± 0.040 respectively where the error is given

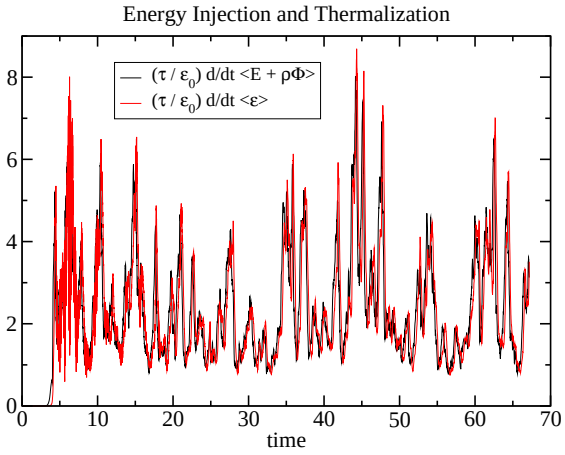

FIGURE 5. Time evolution of the time derivative of the volume averaged total energy and thermal energy. This figure demonstrates a clearly discernible delay between the energy injection and thermalization rate. Time is in units of the orbital period.

by one standard deviation. These values are approximately 4 times larger than for the mean toroidal field configuration. The ratio of the Maxwell to Reynolds stress is 6.4. These numbers are in good agreement with [13].

The evolution of the volume averaged internal energy $< \varepsilon >$ in figure 3 shows approximately a factor of 7 times larger heating rate than was found in [13]. It is interesting to note that the time variability of the Maxwell and Reynolds stress in these flows is sufficiently large that it results in a clearly discernible stair stepping on the evolution of the total and internal energy density.

It was shown in [18] that the presence of recurrent channel flows results in a clearly observable time delay between the time derivative of the volume average of the total energy $< E + \rho\Phi >$ and the time derivative of the volume average of the thermal energy density $< \varepsilon >$. Note that these quantities are equivalent to the energy injection rate and the energy thermalization rate. Differentiating the total and thermal energy plots in figure 3 and normalizing the derivative to the ratio of the initial thermal energy density and the orbital period, one obtains an equivalent plot, shown in figure 5, to that presented in [18]. Despite the presence of high frequency oscillations in the thermal energy evolution (which are a result of magnetosonic oscillations) there is a clearly discernible time lag between the peak in the energy injection rate and the average turbulent dissipation rate. The results presented in figure 5 also agree with [18] in that the thermalization rate overshoots the energy injection rate at its maximum. The fact that the results presented here are for an ideal MHD fluid, while those in [18] are for a magnetic Reynolds number $\mathrm{Re}_M = 1$ provides strong support for both calculations. The time lag between the energy injection rate and thermalization rate is a direct result of the channel flows and is essentially independent of the nature of the resistivity. Note that this delay is not observed for any other field configuration.

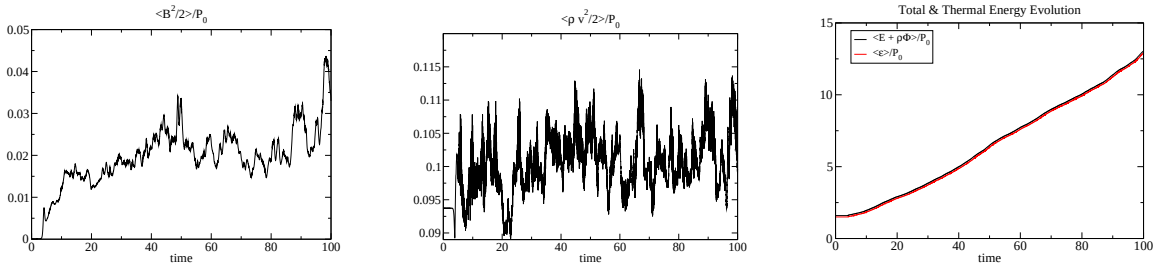

FIGURE 6. Time evolution of the volume averaged magnetic, kinetic, total and thermal energy for the zero net field calculation S2. Time is in units of the orbital period.

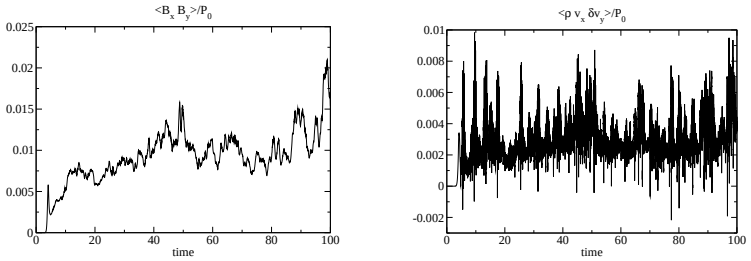

FIGURE 7. Time evolution of the volume averaged Maxwell and Reynolds stress for the zero net field calculation S2. Time is in units of the orbital period.

Zero Net Flux

Next we consider the case where the magnetic field is initialized with $B_x = B_y = 0$ and $B_z = B_0 \sin(2\pi x/L_x)$ with $\beta = 2P/B_0^2 = 4000$. It was shown in [19] that the saturation of the MRI is independent of the initial value of β. As a result, this model calculation can be compared to the results of models SZ1, SZ2 and SZ3 in [19]. In figure 6 we present the temporal evolution of the volume averaged kinetic, magnetic, thermal and total energies, and in figure 7 the Maxwell and Reynolds stress. The volume averaged Maxwell stress $< -B_x B_y > /P_0$ and Reynolds stress $< \rho v_x \delta v_y > /P_0$ have a mean value of $9.5 \times 10^{-3} \pm 2.8 \times 10^{-3}$ and $2.9 \times 10^{-3} \pm 1.3 \times 10^{-3}$ respectively where the error is given by one standard deviation. These values are approximately 4 times smaller than for the mean toroidal field configuration. The saturation amplitude of the magnetic energy density agrees well with the results of [19]. Another feature of these flows is that they strongly excite compressional fast magnetosonic waves which propagate both inward and outward in the computational domain. These compressional waves are primarily responsible for the rapid time variability in the mean Reynolds stress as shown in figure 7. The presence of these waves was also noted in [19].

Compressibility Effects

A rather dominant feature which we have observed in our shearing box simulations is the formation of spiral waves and weak shocks. Figure 8 shows an example of a

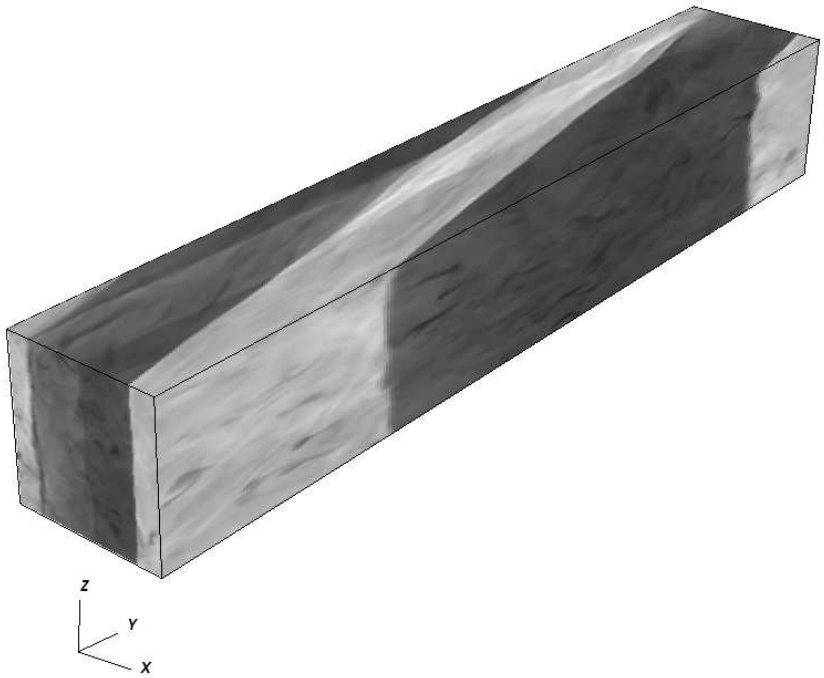

FIGURE 8. Greyscale image of the density in model S0C1 showing the presence of spiral shock waves. The density ranges from 0.8 (black) to 1.2 (white).

weak shock in the density in the model S0C1 calculation described in the following section. Watching the time evolution of the density one finds the recurrent formation of weak spiral shocks which rapidly propagate across the grid, dissipate and at some later time are regenerated. One way to study this phenomena is to look at the probability distribution function (PDF) for the density. Perhaps the most illuminating aspect of the density PDF is the time evolution of the standard deviation as shown in figure 9. The first feature to notice in this figure is that all three models show a rapid increase in the density dispersion as the system makes the transition to a turbulent state followed by a gradual decrease toward some small positive value. Note that the larger the heating rate, the faster the standard deviation of the density decreases. These results support the conclusion that the decrease in the density dispersion as the system evolves is a simple consequence of the increasing thermal energy density driving the system toward the incompressible limit. Calculations initiated with a larger initial pressure also support this conclusion. Interspersed on this plot are regions of rapid variability, which are unresolved in the figure, but have a well defined characteristic period described by fast magnetosonic oscillations with an oscillation period $\tau \approx L_x/c_{fast}$. These coherent magnetosonic oscillations appear to be the direct result of the localized dissipation of magnetic energy in current sheets via “numerical resistivity” and the shearing box boundary conditions which effectively make the shearing box a resonant cavity like structure at wavelengths comparable to the box size. In the Y2 and Z2 models at late times we find that the PDF for the density, temperature, and specific entropy are

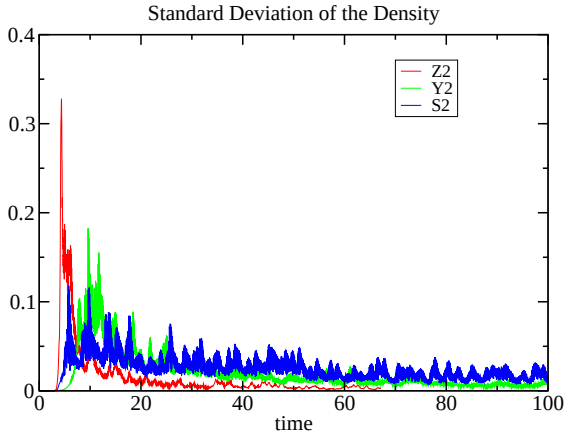

FIGURE 9. Time evolution of the standard deviation of the density PDF for the three adiabatic calculations S2, Y2, and Z2. Time is in units of the orbital period.

well described by a Gaussian distribution. At early times, the density and temperature PDFs for all calculations presented here are highly time variable resulting from the compressible modes in the shearing box.

It is worth pointing out that the initial pressure in the models presented here was selected to correspond to approximately the central 1 scale height of a vertically stratified accretion disk. In a time steady accretion disk calculation, losses due to radiative cooling will balance the turbulent heating and the compressibility will be non-negligible. These results suggest that the localized dissipation of magnetic energy in current sheets and the resulting compressional waves may play an important role determining the temperature fluctuations and hence the spectra of accretion disks.

Radiative Zero Net Flux

In this section we present the results of a zero net flux calculation including radiative cooling. This calculation is identical to the zero net flux calculation presented earlier with the exception that it is resolved on a $128 \times 256 \times 128$ grid. In figure 10 we present the time evolution of the volume averaged kinetic, magnetic, thermal and total energies. The radiative cooling rate was selected in this calculation to match the turbulent heating rate in the saturated state. As a result the total and thermal energy density show little time evolution. Note also the highly time variable kinetic energy density which is a result of the magnetosonic oscillations and spiral shock waves which are present in this calculation. In figure 11 we present the volume average of the Maxwell and Reynolds stress. The volume averaged Maxwell stress $< -B_x B_y > /P_0$ and Reynolds stress $< \rho v_x \delta v_y > /P_0$ have a mean value of $3.2 \times 10^{-3} \pm 1.7 \times 10^{-4}$ and $1.4 \times 10^{-3} \pm 6.4 \times 10^{-4}$ respectively where the error is given by one standard deviation. These values are approximately a half of the values found in the calculations presented earlier at half the resolution. This strong resolution dependence is not found in either the mean toroidal or mean vertical field calculations. Note that these values for the Maxwell and Reynolds

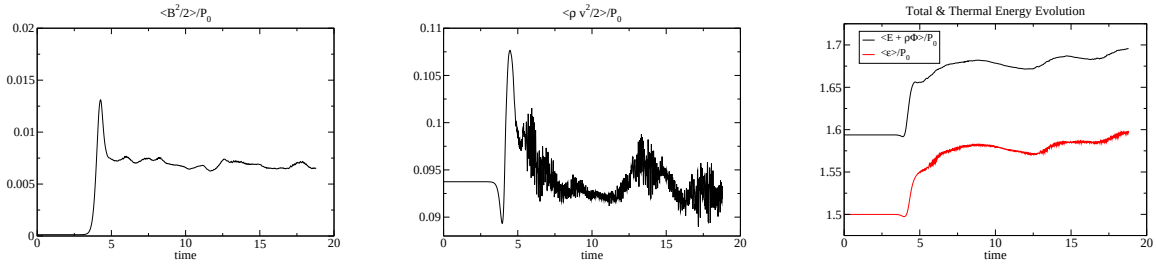

FIGURE 10. Time evolution of the volume averaged magnetic, kinetic, total and thermal energy for the zero net field calculation S0C1. Time is in units of the orbital period.

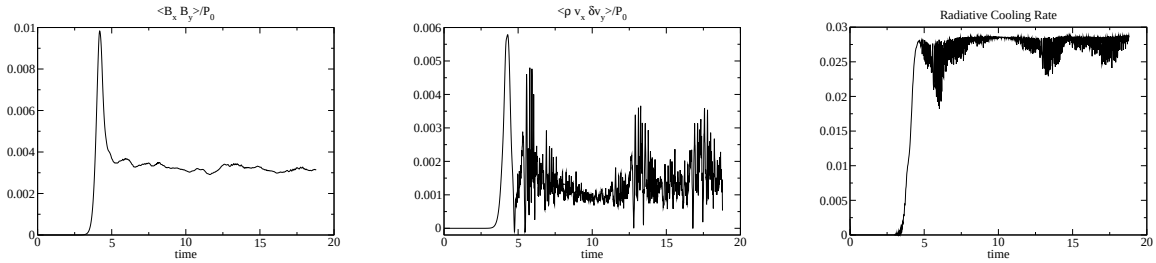

FIGURE 11. Time evolution of the volume averaged Maxwell and Reynolds stress and the radiative cooling rate for the zero net field calculation S0C1. Time is in units of the orbital period and the radiative cooling rate is in units of (ε_0/τ), the initial internal energy divided by the orbital period.

stress are not a result of the presence of radiative cooling in these calculations, as we have also performed non-radiative calculations at this resolution and find essentially identical values.

In figure 11 we present the volume averaged radiative cooling rate in units of (ε_0/τ), the ratio of the initial internal energy density to the orbital period. Note that, as a consistency check, one can relate the radiative cooling rate the the mean Maxwell and Reynolds stress shown in figure 11 via equation (7) under the assumption that the turbulent heating is balanced by the radiative cooling. As should be expected, one finds a very good agreement from this test. There are two main features present in this plot, the rapid rise as the system makes the transition to the turbulent state, and the oscillations resulting from the compressional magnetosonic waves and spiral shocks. While the high frequency oscillations are strongly determined by the boundary conditions of the shearing box, it is suggestive that the coupling of compressional modes to radiative losses may have an impact on the observed spectrum from accretion disks.

CONCLUSIONS

We have performed a series of shearing box calculations for three different field geometries with the recently developed simulation code Athena. This is the first time that a fully second order accurate Godunov algorithm has been applied to the study of the magnetorotational instability in the shearing box formalism. As such, comparing the calculations presented here to previously published results provides an independent confir-

mation. In general we have found that for non-radiative calculations the saturation amplitudes of the magnetic and kinetic energy, the Maxwell and Reynolds stress are in good agreement with the results published in [13, 19]. We also found from the non-radiative calculations that the energy dissipation rate is underestimated in [13] and presumably also in [19] by a factor of $7-10$. This difference is likely attributable to the lack of a resistive heating term in the evolutionary equation for the internal energy.

One of the consequences of energy conservation is the accurate treatment of the dissipation of magnetic energy into thermal. This has been found to influence the solution in the shearing box in two ways. The first is the secular heating of the plasma as must occur since over a long time average the energy injection and thermalization rates must balance. This has the tendency to push the system toward an incompressible configuration in which the PDF of the thermodynamic variable tends toward a Gaussian distribution. The second is the generation of compressible magnetosonic waves and spiral shocks. This is presumably a result of the fact that in ideal MHD calculations the numerical resistivity is nonlinear leading to the dissipation of the magnetic field predominantly in the form of current sheets. This localized heating process generates compressional waves which effectively resonate in the shearing box. These compressional modes, which are most important at early times, have a strong influence on the PDF for the density and temperature in these simulations. In radiatively cooling calculations they also have a direct influence on the radiative cooling rate. These results are suggestive that magnetic field dissipation in current sheets and the resulting compressional modes may have an observable influence on an accretion disk spectrum.

We have also observed the recurrent channel solutions in simulations with a mean vertical magnetic field and the associated time lag between the energy injection rate and energy thermalization rate described in [18]. The fact that the calculations presented here were performed with ideal MHD, while those in [18] have a magnetic Reynolds number $\mathrm{Re}_M = 1$ provides strong support that these results are essentially independent of the magnetic resistivity, so long as the MRI can operate.

The energetics of turbulent accretion disks remains one of the least well explored and most fruitful areas for future research in accretion physics. Not only does an accurate treatment of the energetics allow for contact between theoretical models and observations, but it also allows us to study the way in which the highly nonlinear temperature dependence of the resistivity, Hall and ambipolar diffusion terms influence the the nonlinear behavior of the MRI. These results hold potentially significant promise for improving our understanding of the accretion process in protostellar accretion disks and outburst phenomena in dwarf nova disks. Even the modest question of how the interplay between radiative cooling and turbulent heating influence the vertical structure of an accretion disk remains an open question.

ACKNOWLEDGMENTS

The calculations presented here were performed on the beowolf cluster in the Princeton dept. of Astrophysical Sciences. We would like to acknowledge the support of the NSF grant AST-0216105.

REFERENCES

1. S. A. Balbus, and J. F. Hawley, *Reviews of Modern Physics*, **70**, 1–53 (1998).
2. S. A. Balbus, "Numerical Simulations of the MRI and Real Disks," in *Astronomical Society of the Pacific Conference Series*, 2005, vol. CS-330, astro-ph/0411281.
3. S. A. Balbus, and J. F. Hawley, *Lecture Notes in Physics, Berlin Springer Verlag*, **614**, 329–348 (2003).
4. S. A. Balbus, ARA&A, **41**, 555–597 (2003).
5. A. Brandenburg, A. Nordlund, R. F. Stein, and U. Torkelsson, ApJ, **446**, 741–754 (1995).
6. W. Kim, and E. C. Ostriker, ApJ, **540**, 372–403 (2000).
7. T. Sano, S. Inutsuka, N. J. Turner, and J. M. Stone, ApJ, **605**, 321–339 (2004).
8. J. M. Stone, C. F. Gammie, S. A. Balbus, and J. F. Hawley, *Protostars and Planets IV*, pp. 589–611 (2000).
9. M. W. Kunz, and S. A. Balbus, MNRAS, **348**, 355–360 (2004).
10. C. F. Gammie, and K. Menou, ApJ, **492**, L75–L78 (1998).
11. T. Sano, and J. M. Stone, ApJ, **586**, 1297–1304 (2003).
12. T. A. Gardiner, and J. M. Stone, J. Comput. Phys., **205**, *in press* (2005).
13. J. F. Hawley, C. F. Gammie, and S. A. Balbus, ApJ, **440**, 742–763 (1995).
14. P. Collela, J. Comput. Phys., **87**, 171–200 (1990).
15. J. Saltzman, J. Comput. Phys., **115**, 153–168 (1994).
16. P. Collela, and P. R. Woodward, J. Comput. Phys., **54**, 174–201 (1984).
17. C. R. Evans, and J. F. Hawley, ApJ, **332**, 659–677 (1988).
18. T. Sano, and S. Inutsuka, ApJ, **561**, L179–L182 (2001).
19. J. F. Hawley, C. F. Gammie, and S. A. Balbus, ApJ, **464**, 690–703 (1996).